

Viscoelastic film flows over an inclined substrate with sinusoidal topography. I. Steady state

D. Pettas,¹ G. Karapetsas,² Y. Dimakopoulos,¹ and J. Tsamopoulos^{1,*}

¹Laboratory of Fluid Mechanics and Rheology, Department of Chemical Engineering,
University of Patras, Patras GR-26500, Greece

²Department of Chemical Engineering, Aristotle University of Thessaloniki, Thessaloniki GR-54124, Greece



(Received 6 March 2019; published 8 August 2019)

We consider the steady flow of a viscoelastic liquid film over an inclined wall with sinusoidal corrugations of arbitrary wavelength and depth. We develop a computational model and carry out detailed numerical simulations based on the finite-element method to investigate this flow. To this end, we solve the two-dimensional momentum and mass conservation equations while employing the Phan-Thien-Tanner (PTT) constitutive model to account for the rheology of the viscoelastic material. An elliptic grid generation scheme is used to follow the large deformations of the liquid film. We perform a thorough parametric analysis to investigate the combined effects of elasticity, inertia, and capillary and viscous forces on the characteristics of the steady flow. The results of our simulations indicate that fluid elasticity suppresses interfacial deformation at low flow rates, whereas at moderate values of Re it enhances the deformation considerably. In the latter case, elastic forces may even give rise to the formation of a static hump and a cusp at the free surface, the size of which increases with the relaxation time of the liquid. The resonance of the liquid film with the substrate undulations is also enhanced by shear thinning. Interestingly, it is predicted that under certain conditions the transition to the inertia regime is not smooth and a hysteresis loop arises, which is the signature of an abrupt change of the film shape, since its high deformations cannot be sustained. Additionally, we have performed calculations for a wide range of different geometrical characteristics of the substrate. We find that viscoelastic effects become more pronounced in the case of long-wavelength wall undulations, while for substrates with short wavelengths the effect of shear thinning is less significant due to the presence of vortices inside the corrugations.

DOI: [10.1103/PhysRevFluids.4.083303](https://doi.org/10.1103/PhysRevFluids.4.083303)

I. INTRODUCTION

Film flows, which are driven by a body force (such as gravity or centrifugal force) flowing down an inclined plane, have drawn considerable attention over the last decades with increasing interest due to their broad spectrum of applications which scales from micro to macro [1]. Some prominent examples include spin coating [2], gravure printing [3], heat exchangers, and adsorption or distillation columns using structured packings [4], mudslides, and lava flows [5], while thin films are also connected with the wettability and the spreading of fluids over substrates [6]. In practice, however, the substrates encountered are never completely flat since they may contain well-defined features in the form of sharp steps, trenches, pillars, corrugations, etc., while irregularities may also arise due to the presence of arrested drops and particles on the substrate. A common difficulty that arises is that these topographic irregularities of the substrate induce variations in the thickness of

*tsamo@chemeng.upatras.gr

the deposited layer. In such types of flows, the liquids involved may often be a polymeric solution or a suspension of particles which in general exhibit non-Newtonian properties. The rheology of the material may considerably affect the flow, introducing interesting effects on the flow arrangement and the film shape. Our goal is to thoroughly investigate the effect of the elastic, viscous, capillary, and inertia forces on the flow characteristics of a viscoelastic liquid flowing over a wavy substrate of different sizes.

Through the years, a large amount of work has been devoted to the study of film flow over structured surfaces, either through experimental [4,7–9] or theoretical studies [10–12]. An early attempt to address this problem theoretically was made by Pozrikidis [13] who studied the two-dimensional (2D) flow over a wavy wall using the integral boundary method under the Stokes flow assumption. The same method was later used by Mazouchi and Homsy [12] for the study of 2D flow inside and out of a square trench and by Blyth and Pozrikidis [14] for examining the flow over a three-dimensional (3D) obstacle attached on the substrate. Alternatively and more frequently in semianalytic studies, the lubrication (long-wave) approximation has been employed using topography adjusted models to approximate the sharp and nearly rectangular indentations of the wall; however, these models are limited to low values of Ca . Such an approach was followed by Stillwagon and Larson [2] who invoked the lubrication approximation to determine the film thickness variation over a trench as it arises in spin coating. Kalliadasis *et al.* [11,15] used the lubrication theory to study the flow of a thin film over a trench as an example of a one-dimensional localized topographical feature. They found that the dynamics of the film is governed by the geometric characteristics of the obstacle. They showed that the free surface developed a capillary ridge before a step-down and a depression region before the step-up of the trench.

The limitations of the former approaches, using the long-wave approximation, were investigated by Gaskell *et al.* [10] and Veremieiev *et al.* [16] by actually solving the exact Navier-Stokes equations in the presence of 2D square trenches. The transition from creeping flow to inertial flow was studied numerically by Bontozoglou and Serifi [17] for film flows along a vertical substrate with isolated, deep step changes. They showed that the capillary ridge before a step-down and the capillary depression before a step-up change their streamwise length scale in the presence of inertia. Their analysis, based on order-of-magnitude arguments of the gravity, capillary, and inertia terms in the momentum balance, also demonstrated that the computed streamwise length of the capillary ridge or depression decreases with increasing flow rate. Later, Wierschem *et al.* [18] and Nguyen and Bontozoglou [19] numerically solved the steady flow of a liquid film along a sinusoidal corrugated wall with small and finite wall amplitude, respectively. Both studies assumed that the steady flow has the same period with the wall undulations while demonstrating that resonance is possible between the substrate and the free surface. Moreover, the existence of nonlinear resonance has been examined by Heining *et al.* [20], who showed the emergence of higher harmonics on a film surface flowing over a wavy wall for low-viscosity liquids. Interestingly, Tseluiko *et al.* [21] showed that under certain conditions and depending on the wall period, a gravity-driven film may undergo a sequence of saddle-node bifurcations revealing steady states with different periodicity than the wall period. In all the above studies, the liquid was considered to wet the solid structure fully. However, a fully wetting state cannot always be achieved, and in many cases, air may be entrapped inside the topographical features, for example, when the surfaces are hydrophobic and/or the amplitude of the substrate variation exceeds a critical value [22–25].

In coating applications, the flowing material is often a polymer solution or a suspension of particles, which in most cases exhibit non-Newtonian properties. Although it is understood that the complex rheological behavior may introduce interesting phenomena affecting the flow arrangement, the film shape, and the stability of the fluid flow, a limited number of related studies appear to date in the literature. The first attempt was made by Saprykin *et al.* [26], who studied the case of liquids following the Oldroyd-B model while employing the long-wave approximation. They examined the interaction of fluid elasticity with inertia, albeit due to the restrictions of their approach they focused on weakly viscoelastic liquids. More recently, Pavlidis *et al.* [27,28] considered a viscoelastic film flowing over periodic rectangular trenches. Since they solved the 2D momentum equations, they

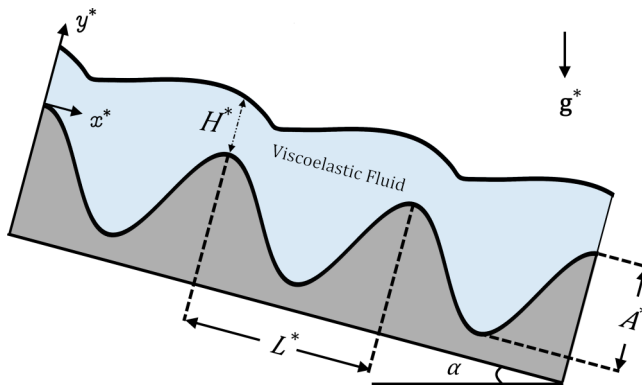


FIG. 1. Cross section of the film flowing over a sinusoidal substrate inclined with respect to the horizontal by an angle α . L^* and A^* are the length and the depth of the unit cell of the substrate, respectively. H^* is the film height at the inlet of the periodic unit cell.

were able to account for highly viscoelastic liquids (employing the exponential form of the PTT (ePTT) model [29]) and to study the effects of inertia and elasticity even for very steep geometries.

The goal of the present study is to examine the steady flow of viscoelastic films flowing over surfaces with sinusoidal corrugations of arbitrary depth. To this end, we consider a viscoelastic liquid that follows the ePTT constitutive law which allows a realistic variation of the shear and extensional fluid viscosities with the local rate of strain components as encountered in typical polymeric solutions. We will solve the 2D momentum balance and constitutive equations for the velocities and viscoelastic stresses without making any restricting assumptions. In Part II of this work [30], we will perform a linear stability analysis considering as base state the steady solution that is derived in Part I by employing the Floquet-Bloch theory and assuming that the steady solution is subjected both to 2D and 3D disturbances of an arbitrary wavelength.

The rest of this paper is organized as follows: In Sec. II, we present the problem formulation, while in Sec. III, we briefly discuss the solution method used. In Sec. IV, we validate our numerical code by comparing its predictions with theoretical and experimental studies for Newtonian liquids. In Sec. V, we present the numerical results for the effect of elasticity, shear thinning, zero-shear viscosity, and the influence of the substrate geometry on the fluid flow. Finally, concluding remarks are given in Sec. VI.

II. PROBLEM FORMULATION

We consider the steady free surface flow of a viscoelastic liquid film driven by gravity along an inclined sinusoidally corrugated substrate normal to the main flow direction (see Fig. 1). This substrate is the prototypical shape of a periodic rough surface and is frequently used in both experiments and theoretical analysis [19,31,32]. In what follows, the superscript “*” will indicate a dimensional quantity. The function that describes the shape of the wall is given by the following expression:

$$f_{\text{Wall}}^*(x^*) = \frac{A^*}{2} \left[\cos\left(\frac{2\pi x^*}{L^*}\right) - 1 \right], \quad (1)$$

where L^* and A^* are the dimensional length and depth of the unit cell. The liquid is considered to be incompressible, with constant density ρ^* , surface tension σ^* , relaxation time λ_e^* , and total zero-shear viscosity $\mu^* = \mu_p^* + \mu_s^*$, where μ_s^* and μ_p^* are the viscosities of the solvent and the polymer, respectively. The primitive flow input is the volumetric flow rate per unit length normal to the film cross section at the inlet, q^* . The flow is described using a Cartesian coordinate system

TABLE I. Table of dimensionless parameters of the problem and their representative values.

Name	Symbol	Definition	Representative values
Reynolds number	Re	$\frac{\rho^* q^*}{\mu^*}$	0 – 30
Stokes number	St	$\frac{\rho^* g^* H_N^{*2}}{\mu^* U_N^*}$	3/ sin α
Kapitza number	Ka	$\frac{\sigma^* \rho^{*1/3}}{g^{*1/3} \mu^{*4/3}}$	1 – 10
Capillary number	Ca	$\frac{\mu^* q^*}{\sigma^* \eta_N^*}$	0 – 0.35
Weissenberg number	Wi	$\frac{\lambda_e^* q^*}{H_N^{*2}}$	0 – 2.5
Inclination angle	a		10° – 40°
Viscosity ratio	β	$\frac{\mu_s^*}{\mu}$	0.1 – 0.4

with its origin located at the entrance of the flow domain, with the x axis and y axis in the direction parallel and normal to the wall at $x = 0$, respectively (see Fig. 1).

We scale all the lengths with the film thickness of the Nusselt flow H_N^* and all the velocity components with the mean Nusselt film velocity U_N^* , defined as

$$H_N^* = q^{*1/3} \left(\frac{3\mu^*}{\rho^* g^* \sin \alpha} \right)^{1/3}, \quad U_N^* = q^{*2/3} \left(\frac{\rho^* g^* \sin \alpha}{3\mu^*} \right)^{1/3}. \quad (2)$$

Both pressure and stress components are scaled with a viscous scale, $\mu U_N^*/H_N^*$. Thus, the dimensionless numbers that arise in the problem and the corresponding representative values are given in Table I. Due to the specific choice of the characteristic length, velocity, and inclination angle, the value of the Stokes number is constant.

A. Governing equations

The two-dimensional steady-state flow is governed by the laws of momentum and mass conservation:

$$\text{Re}(\mathbf{u} \cdot \nabla \mathbf{u}) + \nabla P - \nabla \cdot \boldsymbol{\tau} - \text{St} \mathbf{g} = \mathbf{0}, \quad (3)$$

$$\nabla \cdot \mathbf{u} = 0, \quad (4)$$

where $\mathbf{u} = (u_x, u_y)^T$, P , and $\boldsymbol{\tau}$ denote the velocity, pressure, and stress fields, respectively, and $\nabla = (\partial_x, \partial_y)^T$ denotes the gradient operator for Cartesian coordinates. We also define the unit gravity vector as $\mathbf{g} = (\sin a, -\cos a)^T$. The extra stress tensor $\boldsymbol{\tau}$ is split into a purely Newtonian part $2\beta \dot{\boldsymbol{\gamma}}$ and a polymeric contribution $\boldsymbol{\tau}_p$,

$$\boldsymbol{\tau} = 2\beta \dot{\boldsymbol{\gamma}} + \boldsymbol{\tau}_p, \quad (5)$$

where $\dot{\boldsymbol{\gamma}} = \frac{1}{2}(\nabla \mathbf{u} + \nabla \mathbf{u}^T)$ is the rate of strain. To account for the viscoelasticity of the material, we use the affine exponential form of the Phan-Thien and Tanner model [29]:

$$Y(\boldsymbol{\tau}_p) \boldsymbol{\tau}_p + Wi \overset{\nabla}{\boldsymbol{\tau}}_p - 2(1 - \beta) \dot{\boldsymbol{\gamma}} = 0, \quad Y(\boldsymbol{\tau}_p) = \exp \left(\frac{\varepsilon}{1 - \beta} Wi \text{trace}(\boldsymbol{\tau}_p) \right), \quad (6)$$

where $\overset{\nabla}{\boldsymbol{\tau}}_p = \mathbf{u} \cdot \nabla \boldsymbol{\tau}_p - \boldsymbol{\tau}_p \cdot \nabla \mathbf{u} - (\boldsymbol{\tau}_p \cdot \nabla \mathbf{u})^T$ is the upper convective derivative of $\boldsymbol{\tau}_p$. The viscoelastic fluid properties depend on the dimensionless parameters Wi, β , and ε . Finite values of the parameter ε set an upper limit to the elongational viscosity, which increases as the parameter decreases, while it introduces elongational and shear thinning to the fluid model. The predictions for the elongational and shear viscosity of this model for various values of ε appear in Fig. 9 of [33].

Clearly, the ePTT model reduces to the Oldroyd-B model by setting ε equal to zero and the Upper Convective Maxwell (UCM) model by additionally setting $\beta = 0$.

B. Boundary conditions

Along the air-liquid interface, we apply the following interfacial stress balance:

$$\mathbf{n} \cdot (-P\mathbf{I} + \boldsymbol{\tau}) = \frac{\kappa}{Ca} \mathbf{n}, \quad (7)$$

where \mathbf{n} is the outward unit normal vector to the free surface and κ is the mean curvature defined as

$$\kappa = -\nabla_s \cdot \mathbf{n}, \quad \nabla_s = (\mathbf{I} - \mathbf{nn}) \cdot \nabla. \quad (8)$$

Note that in Eq. (7) the ambient pressure has been set equal to zero (datum pressure) without loss of generality. The capillary number, Ca , naturally arises in the interfacial stress balance; however, for the discussion that follows it will be dropped in favor of the Kapitza number, which depends only on material properties, see Table I:

$$Ka = \frac{\sigma^* \rho^{*1/3}}{g^* \mu^{*4/3}} \equiv \left(\frac{l_c^*}{l_v^*} \right)^2, \quad (9)$$

where l_c^* and l_v^* are the capillary length and viscous length, respectively, defined as

$$l_c^* = \left(\frac{\sigma^*}{\rho^* g^*} \right)^{1/2}, \quad l_v^* = \left(\frac{\mu^{*2}}{\rho^{*2} g^*} \right)^{1/3}. \quad (10)$$

Although the Kapitza number depends on three different liquid properties, we should keep in mind that in practical applications its variation is mostly due to the variations in liquid viscosity. This is because surface tension and density of most common polymeric solutions vary in a much shorter range. Moreover, Ka is not an independent number but can be related to the previously introduced dimensionless quantities via the following expression:

$$Ka = Ca^{-1} St^{-1/3} Re^{2/3}. \quad (11)$$

Along the free surface, we also impose the kinematic condition

$$\mathbf{n} \cdot \mathbf{u} = 0, \quad (12)$$

while along the walls of the substrate, we impose the usual no-slip, no-penetration boundary conditions. Additionally, we impose periodic boundary conditions in the velocity and stress field between the inflow and the outflow of the domain. Note that for the purposes of the present study we assume that the steady flow has the same periodicity as the substrate structure (i.e., we assume that the steady solution is L periodic):

$$\mathbf{u}|_{x=0} = \mathbf{u}|_{x=L}, \quad (13)$$

$$\mathbf{n} \cdot (-P\mathbf{I} + \boldsymbol{\tau})|_{x=0} = \mathbf{n} \cdot (-P\mathbf{I} + \boldsymbol{\tau})|_{x=L}. \quad (14)$$

Finally, the film height at the entrance of the unit cell H^* is determined by requiring that the dimensionless flow rate is equal to unity:

$$q = \int_0^{H^*/H_N^*} u_x dy = 1. \quad (15)$$

C. Alternative length scaling

According to our scaling, the dimensionless lengths that arise in the problem are H^*/H_N^* and L^*/H_N^* . It is important to note, though, that with these definitions the dimensionless lengths under

different flow conditions will depend on the value of the Nusselt film height H_N^* [see Eq. (2) and Table I], which depends both on the properties of the liquid and the flow rate. The dependence on the latter may introduce some difficulties in the interpretation of the results, and therefore it is preferable to use an alternative scaling for the lengths based on the capillary length l_c^* , which depends only on the liquid properties; a similar approach was also used by Trifonov [34]. The following expression relates the Nusselt film height to the capillary length l_c^* :

$$H_N^* = l_c^* \text{Ka}^{-1/2} \text{Re}^{1/3} \text{St}^{1/3}. \quad (16)$$

By rescaling all lengths with the capillary length, we keep the dimensionless lengths of the geometry independent of the Reynolds number, and the relation between the new and the original scaling is given by

$$\left(\frac{H^*}{H_N^*}, \frac{L^*}{H_N^*} \right) \equiv \left(\frac{H^*}{l_c^*}, \frac{L^*}{l_c^*} \right) l_{\text{ratio}}, \quad l_{\text{ratio}} = \text{Ka}^{1/2} \text{Re}^{-1/3} \text{St}^{-1/3}. \quad (17)$$

For the discussion that follows, we choose as a base case the Newtonian properties of Elbesil 65 ($\mu^* = 62.4$ mPa s, $\rho^* = 958.5 \frac{\text{kg}}{\text{m}^3}$, and $\sigma^* = 19.91$ mN/m²) flowing over a substrate with $L^* = 20$ mm and $A^* = 8$ mm. The corresponding dimensionless numbers are $\text{Ka} = 3.75$, $L = 13.765$, and $A = 5.506$. These parameter values as well as the inclination angle $\alpha = 10^\circ$ will be kept fixed unless stated otherwise.

III. NUMERICAL IMPLEMENTATION

In order to solve accurately and efficiently the above set of equations, we employ the Discrete Elastic Viscous Split Stress (DEVSS-G) method that has been successfully used in the past for the solution of viscoelastic flows [35]. Thus, after reformulating the momentum and constitutive equations we obtain

$$\text{Re}(\mathbf{u} \cdot \nabla \mathbf{u}) - \text{St} \mathbf{g} + \nabla \text{P} - \nabla \cdot \boldsymbol{\tau}_{DEVSS} = \mathbf{0}, \quad (18)$$

$$Y(\boldsymbol{\tau}_p) \boldsymbol{\tau}_p + Wi[\mathbf{u} \cdot \nabla \boldsymbol{\tau}_p - \boldsymbol{\tau}_p \cdot \mathbf{G} - (\boldsymbol{\tau}_p \cdot \mathbf{G})^T] - (1 - \beta)(\mathbf{G} + \mathbf{G}^T) = \mathbf{0}, \quad (19)$$

where $\boldsymbol{\tau}_{DEVSS} = \boldsymbol{\tau}_p - 2(1 - \beta)\dot{\boldsymbol{\gamma}} + (\mathbf{G} + \mathbf{G}^T)$, and \mathbf{G} is the continuous approximation of the velocity gradient tensor $\nabla \mathbf{u}$.

To solve numerically the above set of equations we employ the mixed finite-element–Galerkin method and approximate the velocity and the position vector with six-node Lagrangian basis functions while the pressure, elastic stresses, as well as the velocity gradients are approximated with three-node Lagrangian basis functions. Due to the hyperbolic character of the constitutive equation and to preserve the numerical stability of the scheme, we also employ the streamline upwind Petrov-Galerkin (SUPG) method [36] introducing the corresponding basis functions.

To account for the deformations of the flow domain, we employ a robust elliptic grid generation scheme. The mesh is generated by solving a system of two quasielliptic partial differential equations [see Eqs. (20) and (21)] which map the physical domain (x, y) to the computational domain (ξ, η) , and it is dynamically adapted to the deforming liquid domain. The mesh generation equations are

$$\nabla \cdot \left\{ \left[\varepsilon_1 \sqrt{\frac{x_\eta^2 + y_\eta^2}{x_\xi^2 + y_\xi^2}} + (1 - \varepsilon_1) \right] \nabla \xi \right\} = 0, \quad (20)$$

$$\nabla \cdot \left\{ \left[\varepsilon_2 \sqrt{\frac{x_\xi^2 + y_\xi^2}{x_\eta^2 + y_\eta^2}} + (1 - \varepsilon_2) \right] \nabla \eta \right\} = 0, \quad (21)$$

where the parameters ε_1 and ε_2 control the smoothness and orthogonality of the mesh lines, and ε_1 , ε_2 are selected by trial and error. This is a very robust method which has been applied successfully to a variety of problems, e.g., see [22,25,37–39], suitable for highly deforming domains. The interested

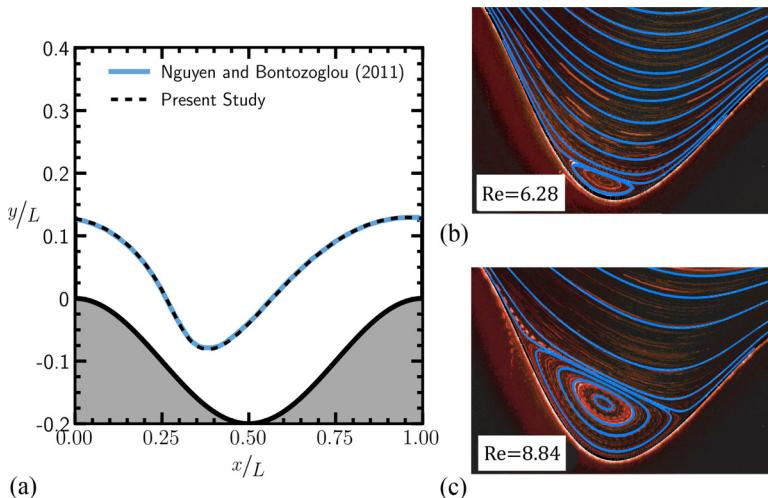


FIG. 2. Comparison of our predictions for an inclined substrate at $\alpha = 45^\circ$ with previous studies by Nguyen and Bontozoglou [19] for $Re = 25$, $Ka = 200$, $A = 5.97$, and $L = 29.87$. (b), (c) Experimental (red lines) [31] and theoretical (blue lines) streamline patterns for Elbesil 145 oil ($Ka = 1.27$) for $Re = 6.28$ and 8.84 , respectively. The inclination angle is $\alpha = 10^\circ$, and geometric characteristics are $L = 13.765$ and $A = 5.506$.

reader may refer to [40] where this method is described in detail. The generated mesh is refined locally with two refinement levels around the free surface of the fluid, as described in [37]. A summary of the weak formulation of the governing equations is presented in the Appendix.

Finally, to trace the steady-state solution in the parameter space, we employ the pseudo-arclength continuation technique [22], which has been incorporated into our in-house finite-element code. According to this method, given an initial solution (\mathbf{q}_0) at an initial parameter value λ_0 , the value of the parameter λ for the next computation is determined as a function of the pseudo-arclength, s . In order to determine λ , an additional equation is obtained by projecting the increment of the augmented solution vector $(\mathbf{q} - \mathbf{q}_0, \lambda - \lambda_0)^T$ on its initial tangent $(\dot{\mathbf{q}}_0, \dot{\lambda}_0)^T$, where the derivatives are taken with respect to s . The product is equal to a specified arclength Δs , resulting in the following additional equation:

$$G(\mathbf{q}, \lambda; \Delta s) := \dot{\mathbf{q}}_0^T \cdot (\mathbf{q} - \mathbf{q}_0) + \dot{\lambda}_0(\lambda - \lambda_0) + \Delta s = 0. \quad (22)$$

In summary, we need to solve the following augmented system of equations (23) and (24) for the augmented solution vector $(\mathbf{q}, \lambda)^T$:

$$\mathbf{F}(\mathbf{q}, \lambda) = 0, \quad (23)$$

$$G(\mathbf{q}, \lambda; \Delta s) = 0, \quad (24)$$

where \mathbf{F} is the system of weighted governing and mesh generating equations, including the extra equation (15). The system of equations (23), (24) is solved by using the Newton-Raphson method.

IV. VALIDATION

Before we proceed with the discussion of our results, we present a series of validation tests of our in-house code against both theoretical predictions and experimental observations for relevant flows that exist in the literature. In Fig. 2(a) we consider the case of a Newtonian fluid ($Wi = 0$) and compare the results of our work with the predictions provided by Nguyen and Bontozoglou [19] for $Re = 25$ and $Ka = 200$. As it can be seen in the figure, the calculated film shapes coincide,

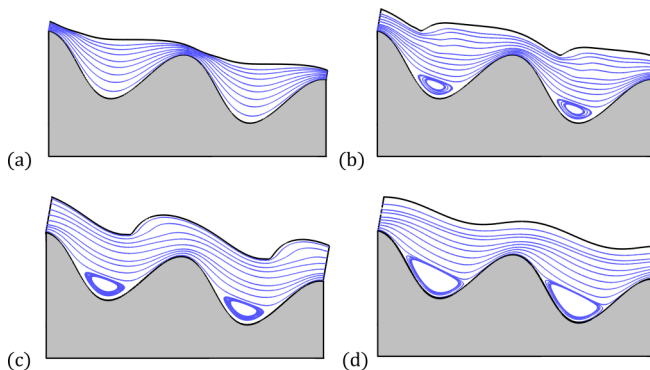


FIG. 3. Streamlines of the steady states of the film flow over the substrate: (a) $Re = 2$, (b) $Re = 8$, (c) $Re = 15$, and (d) $Re = 20$ for $Wi = 1$ and $\varepsilon = 0$.

exhibiting an excellent agreement. An additional confirmation of the accuracy of our computations is provided in Figs. 2(b) and 2(c). This figure presents the streamline pattern obtained using the Particle Image Velocimetry (PIV) technique by Pollak and Aksel [31] for $Ka = 1.27$ and $Re = 6.28$ and 8.84 , respectively, along with the streamlines obtained by our study (shown with the continuous blue lines) calculated at exactly the same flow parameters. As it was noted by Pollak and Aksel [31], the fluid flow can be separated into two zones: the one closer to the air-liquid interface where the flow is gravity driven and another which lies inside the wall corrugations where a recirculation takes place. Note that the two zones cannot communicate with each other, denoting that there is a border between the two regions, forming a separatrix. Clearly, our theoretical results are able to predict all the later phenomena with great accuracy, such as the streamline pattern of the outer flow, the existence of a vortex located in the substrate corrugations which expands with increasing flow rate, as well as the separatrix of the two zones.

V. RESULTS AND DISCUSSION

We begin our discussion by presenting in Fig. 3 the profiles of a viscoelastic liquid film, along with the streamlines, for different values of Re which correspond to different flow rates. With increasing Re , the thickness of the film increases because larger amounts of fluid need to be accommodated due to the higher flow rate. For low values of Re , most of the depression of the film takes place near the upstream wall whereas its position moves downstream with increasing Re . As discussed by Nguyen and Bontozoglou [19], many characteristics of the flow field can be explained by considering the flow as a ballistic flow where the ejection platform for the fluid is the maximum level of the substrate at the inflow. The magnitude of Re determines the distance the fluid can travel before it “lands” somewhere inside the cavity.

At $Re = 2$ and 8 , see Figs. 3(a) and 3(b), the fluid lands closer to the inflow at the descending part of the wall, thus creating a local minimum in film thickness. At intermediate Re , the injected liquid impacts the liquid ahead and with the aid of elasticity forms a cusp, see Figs. 3(b) and 3(c). Above a specific Re , inertia pushes the jet far enough to land at the ascending part of the wall, causing a more prominent hump, see Fig. 3(c). Note that in the case of a Newtonian liquid the interface remains smooth for all values of Re without the presence of a cusp. Thus, the cusp should be attributed to elastic effects. In this case, we also notice the formation of an eddy due to the detachment of fluid in the bottom of the cavity from the main stream of the flow field. With further increase of Re , inertia moves the landing point to the crest of the next corrugation, while the formed eddy extends in size and tends to occupy the entire cavity, see Fig. 3(d).

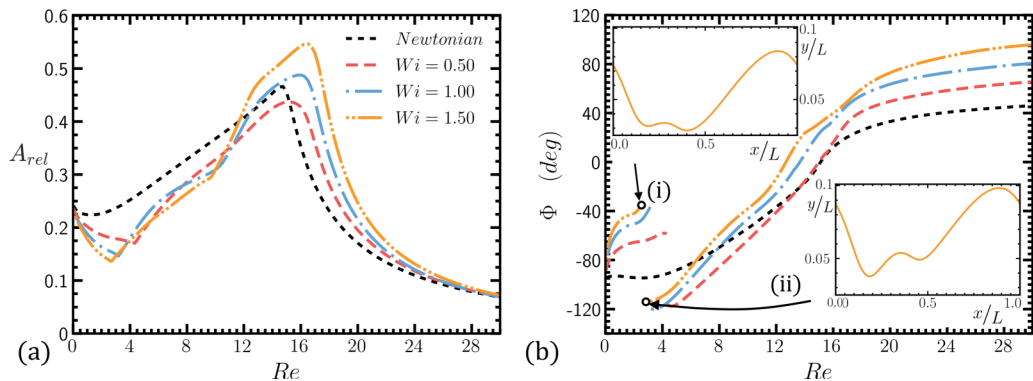


FIG. 4. (a) Relative amplitude of the free surface A_{rel} and (b) the phase shift of the free surface to the wall corrugations as a function of Re for various values of Wi using the Oldroyd-B model ($\varepsilon = 0$). For low Re dual minima appear in the free surface as seen in the insets (i, ii) for $Re = 2.7$ and 2.65 , respectively.

A. Effect of fluid elasticity

The effect of the elastic properties of the fluid on the free surface of the flow is depicted in Figs. 4(a) and 4(b). In this figure we present the relative amplitude of the free surface A_{rel} , which is the ratio of the amplitude of the free surface deformation to the amplitude of the substrate, along with the superficial phase shift, which is measured in terms of the distance in the x direction between the locations of minimum height on the free surface and on the wall (the latter at $x^* = L^*/2$),

$$A_{rel} = \frac{H_{max}^* - H_{min}^*}{A^*}, \quad (25)$$

$$\Phi = 360^\circ \left(\frac{x_{H_{min}}^*}{L^*} - \frac{1}{2} \right), \quad (26)$$

as a function of the Reynolds number for various values of Wi . More specifically, in Fig. 4 we present the relative amplitude and the phase shift of the free surface for $Wi = 0.5, 1.0, \text{ and } 1.5$, while the dashed line shows the case of a Newtonian liquid ($Wi = 0$).

Under creeping flow conditions, due to the high viscous forces the free surface of the fluid nearly follows the shape of the bottom wall, and therefore the relative amplitude of the free surface tends to a small but finite value. Note that for $Re \rightarrow 0$ and when the substrate is aligned with the gravitational force ($\alpha = 90^\circ$), the interface would fully conform with the wall shape and thus $A_{rel} = 1$, whereas for finite inclination angles, as in our case, $A_{rel} \neq 1$ due to the effect of hydrostatic pressure and the smaller gravity force driving the flow. On the other hand, at high inertia the amplitude of the deformation of the free surface tends to zero since the liquid near the interface does not feel the presence of the bottom wall. At intermediate values of the Reynolds number, $2 < Re < 15$, the presence of the substrate structure and the competition between the inertia forces, gravity, and surface tension gives rise to an amplification of the steady free surface deformation. This phenomenon has been confirmed experimentally for the case of Newtonian liquids by Vlachogiannis and Bontozoglou [41] and Argyriadi *et al.* [4] and is often referred to as “resonance” in the literature [42]. This amplification is caused by the interaction between the reflected wave of the free surface with the capillary waves that travel against the flow direction. The point of resonance arises for a particular value of Re for which the surface velocity of the fluid is equal to the phase velocity of the capillary waves. A more recent study by Wierschem *et al.* [18] provides a systematic investigation with arbitrary film thickness and further demonstrates that resonance is associated with the phase locking between the undulated wall and the capillary waves. Furthermore, the existence of the resonant point separates the flow into a subcritical and supercritical regime for lower and higher

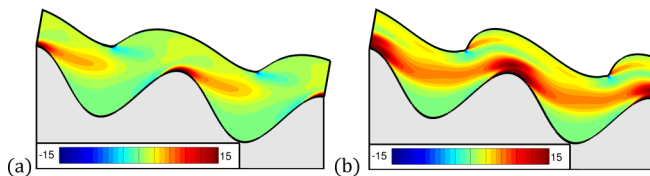


FIG. 5. Spatial variation of the normal stress component ($\tau_{p,xx}$) using the Oldroyd-B model for (a) $Wi = 0.5$ and (b) $Wi = 1.5$ calculated at $Re = 15$.

than the critical values of Re , respectively. In the supercritical regime, the steady free surface is not in phase with the capillary waves and the air-liquid interface appears to be smooth. It has been shown that for Newtonian liquids nonlinear resonance (i.e., when higher harmonics of the free surface take part in the system) is also possible [20] for very high values of Ka ($Ka \approx 2500$). We refrain from examining such effects in the case of viscoelastic liquids, because these are typically high-viscosity liquids with $Ka \leq 20$.

In the case of a viscoelastic fluid, A_{rel} is not affected in the two limiting regimes, i.e., for $Re \rightarrow 0$ and $Re > 25$. For low values of Re , though, even a small amount of elasticity leads to the decrease of A_{rel} as the bulk elasticity of the fluid resists the deformation imposed by the solid wall, see Fig. 4(a) at $Re \cong 2$. For moderate values of Re , the effect of the elasticity has a nonmonotonic impact on the amplification of the steady free surface deformation, close to the resonance point. For weakly viscoelastic liquids, the bulk elasticity tends to suppress the interfacial deformation [see Fig. 4(a) for $Wi = 0.5$]. However, as it is shown in Fig. 4(a), the increase of Wi eventually amplifies the steady free surface deformation (see Fig. 4(a) for $Wi = 1$ and 1.5). This nonmonotonic dependence can be attributed to the formation of a cusp at the liquid-air interface for the case of highly elastic liquids [see Fig. 3(c)].

Moreover, the phase difference between the undulations of the free surface and the wall is depicted in Fig. 4(b). Two limits are identified: at low Re , the phase of the free surface precedes that of the wall, whereas at high Re , it lags behind. It is also noteworthy that in the case of viscoelastic liquids—at low values of Re the free surface exhibits two local minima on the free surface [see insets in Fig. 4(b)] instead of a single depression as in the case of Newtonian liquids. We also observe that for $Wi = 0.50$ and $Re > 4$ the position of the highest depression lies closer to the downstream wall, whereas for $Re < 4$ the local minimum, which lies closer to the upstream wall, becomes more intense; this transition between the two local minima is translated into a discontinuity of the curves for the phase shift for $Re \sim 4$. With increasing elasticity of the liquid, the phase shift Φ increases, indicating that the position of the highest depression migrates towards the downstream wall.

In Figs. 5(a) and 5(b), we present the spatial variation of the xx component of the polymeric stress tensor, for $Wi = 0.5$ and 1.5 , respectively, and for $Re = 15$. The higher the elasticity is, the stronger the stress field is, characterized by a higher stretching of the polymeric chains. The maximum values in the stress field arise at the crest of the substrate where the polymeric chains are extended to conform to the fluid flow, while the stress field is relaxed at the midplane of each cavity where the cross section is larger compared with the inflow and outflow of the sinusoidal domain. The interplay between inertial forces which push the fluid against the downstream wall and the elastic rebound from the wall are responsible for the formation of the cusp and the appearance of an intense static hump next to it, see Fig. 5(b).

B. Effect of shear thinning

Another significant aspect of films which consist of a polymeric solution is the presence of shear thinning. To examine this effect, we present in Fig. 6(a) the relative amplitude of the free surface A_{rel} as a function of Re for various values of ε under constant $Wi = 1$. As mentioned above, the rheological parameter ε of the ePTT model introduces both elongational and shear thinning to the

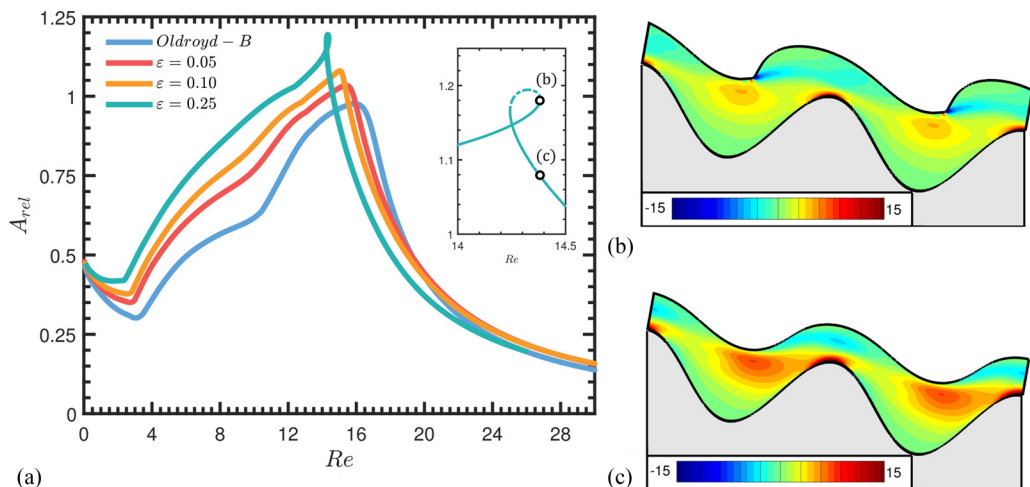


FIG. 6. (a) Relative amplitude of the free surface A_{rel} as a function of the Reynolds number for various values of ϵ at $Wi = 1$. (b), (c) Film shape and spatial variation of shear stress component $(\tau_{p,yx})$ before and after the hysteresis loop, respectively, for $Re = 14.38$, $Wi = 1$, and $\epsilon = 0.25$.

fluid model, while it poses an upper limit to elongational viscosity. In Fig. 6(a), the peak at the resonance point is minimized for the case of the Oldroyd-B model ($A_{rel} = 0.49$ for $\epsilon = 0$), while the maximum value of A_{rel} increases with ϵ . Therefore, from this figure we may deduce that shear thinning enhances the resonant behavior of the steady free surface with the substrate. This finding is also supported by the study of Heining and Aksel [43], who reported that in the case of the generalized Newtonian liquids shear thinning leads to amplification of the free surface, while shear thickening has the opposite effect. We also observe that the peak arises for lower values of Re with increasing ϵ . This effect could be attributed to some extent to the fact that due to shear thinning, viscosity decreases locally and therefore the local Re number is actually higher than the nominal value of Re which is defined based on the zero-shear viscosity.

Interestingly, for highly shear-thinning fluids the transition from the low- Re flow regime to the inertia-dominated regime is not smooth [see Fig. 6(a) for $\epsilon = 0.25$], but two successive turning points exist, creating a hysteresis loop with varying Re between $Re = 14.24$ and 14.38 [see the inset in Fig. 6(a)]. The hysteresis loop indicates that for the same value of Re three different steady states exist; the stability of these solutions will be discussed in the Part II of this study [30]. In Figs. 6(b) and 6(c) we present the spatial variations of the yx component of the polymeric stress tensor for the same $Re = 14.38$ but before (in the ascending part of the continuous line) and after (in the descending part of the continuous line) the hysteresis loop, respectively. Before the hysteresis loop, the effect of fluid elasticity gives rise to the formation of a cusp and a static hump, as in the case of the Oldroyd-B liquid, see Fig. 6(b). The tendency of the cusp to move downstream with increasing Re is inhibited by both the pressure and the normal polymeric stress field generated at the downstream wall. This flow pattern cannot be sustained further, and thus a turning point arises. In Fig. 6(c), we depict the film shape for the latter case, along with contour lines of the polymeric shear stresses. Interestingly, after the hysteresis loop, the flow manages to overpass the wall corrugations without the presence of a cusp, as inertia combined with the increased effect of shear thinning dominate the fluid flow.

C. Effect of zero-shear viscosity and solvent viscosity ratio

In Fig. 7(a) we present the dependence of A_{rel} on the Reynolds number for different values of the Kapitza number. Under constant value of $L = L^*/l_c^*$ and assuming flows over substrates with the

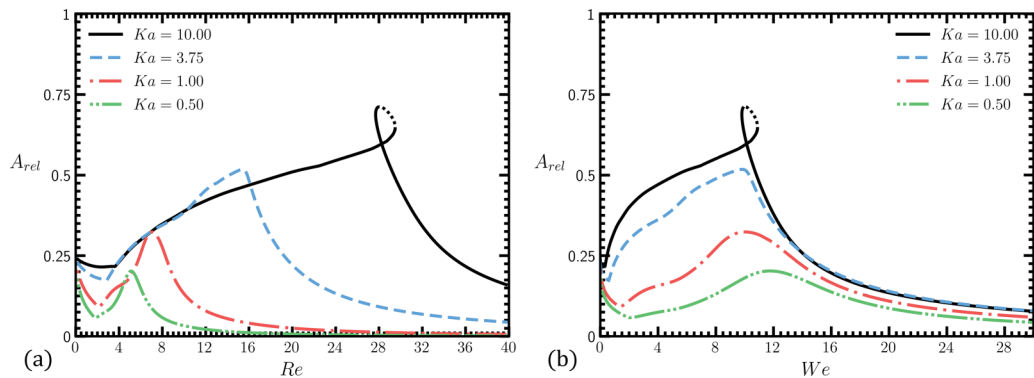


FIG. 7. Relative amplitude of the free surface A_{rel} as a function of (a) Reynolds number and (b) for various values of Ka at $Wi = 1$, $\varepsilon = 0.05$, and $\beta = 0.1$.

same geometrical characteristics, the variation of Ka implies the change of zero-shear viscosity [I_v^* is the only parameter that changes, see Eq. (10)]; therefore smaller values of Ka correspond to liquids with higher viscosity. Thus, with increasing Ka , the film conforms to the shape of the substrate undulations, leading to larger depressions of the liquid-gas interface and intensification of the wall-free surface resonance. As a result, the peak in interfacial deformation grows with increasing Ka . We note that at $Ka = 10$ the transition to an inertia fluid flow regime is not smooth, since a hysteresis loop arises for Re in between $27.7 < Re < 29.5$, indicating that shear-thinning effects come into play. To rationalize this behavior, we have plotted in Figs. 8(a) and 8(b) the shapes of the liquid film for two different values of Ka along with contour lines of the shear stresses. As it is shown in this figure, with increasing Ka the liquid film becomes thinner and therefore for a given flow rate (i.e., constant value of Re) the level of shear stresses increases, leading to more severe shear thinning, which in turn gives rise to the hysteresis loop that appears in Fig. 7 for $Ka = 10$.

We also note that with increasing Ka the point of resonance moves to higher values of Re ; the maximum amplification was calculated at $Re = 5.07$ and 27.94 for $Ka = 0.5$ and 10 , respectively. In Fig. 7(b) we plot the relative amplitude of the free surface as a function of Weber number,

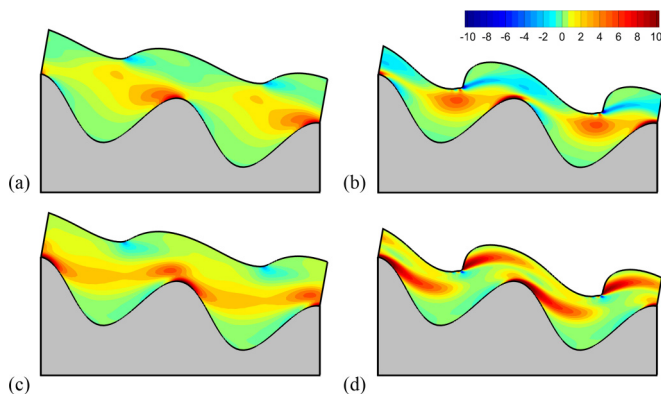


FIG. 8. Film shape and spatial variation of (a), (b) shear stress component ($\tau_{p,yx}$) and (c), (d) normal stress component ($\tau_{p,xx}$). The flow parameters are (a), (c) $Ka = 1.0$ and (b), (d) $Ka = 10$ calculated at $Re = 7.2$ and $Re = 28.7$, respectively, for $Wi = 1$, $\varepsilon = 0.05$, and $\beta = 0.1$.

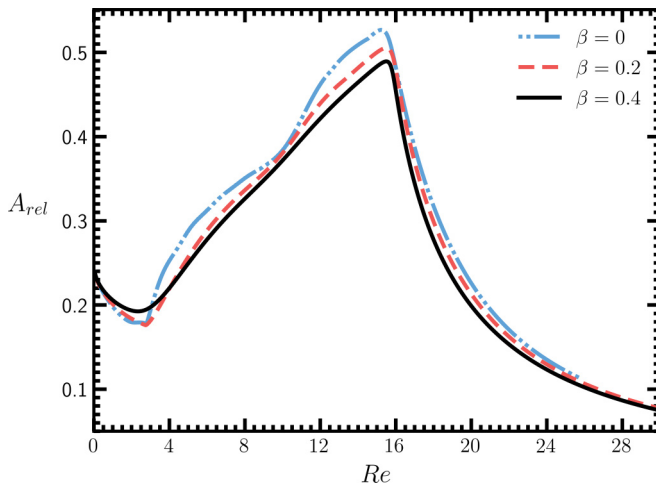


FIG. 9. Relative amplitude of the free surface A_{rel} as a function of Reynolds number for various values of solvent viscosity ratio β for $Wi = 1.0$ and $\varepsilon = 0.05$.

defined as

$$We = \frac{\rho U_N^{*2} H_N^*}{\sigma} \equiv Re Ca, \quad (27)$$

which expresses the ratio of inertia over capillary forces. Interestingly, for moderate to high values of Ka the point of resonance lies close to $We \approx 10$, indicating that the amplification of the standing wave is caused by a delicate balance between inertia and capillary forces. For $Ka = 0.5$, though, the peak arises at slightly higher value of We , i.e., $We = 11.5$. The latter could be attributed to the fact that the film is significantly thicker, see Eq. (16), thus leading to a weaker interaction of the steady free surface with the wavy wall due to the increased distance.

In Figs. 8(c) and 8(d), we additionally examine the spatial variation of the normal polymeric stresses ($\tau_{p,xx}$) for $Ka = 1$ and 10 also calculated at the point of resonance. As it is shown in Fig. 8(c), for $Ka = 1$ (calculated at $Re = 7.2$) the film is quite thick, and the variation of the normal polymeric stresses occurs mostly in an area close to the crest of the substrate where the readjustment of the flow takes place, whereas its variation near the midplane is rather weak. We also note that the pronounced cusp that was observed for $Ka = 3.75$ [see Fig. 3(c)] disappears for low Ka values, see Fig. 8(c). For higher values of Ka , the film becomes thinner and the mean velocity of the fluid increases for a given flow rate. Due to the higher velocities that the liquid experiences, the polymeric chains are extended in the streamwise direction, as suggested by the strong polymeric stress field at the descending part of the wall, shown in Fig. 8(c). Moreover, high values of $\tau_{p,xx}$ also arise adjacent to the cusp near the ascending part of the wall due to the elastic rebound that takes place in this region. As shown in Fig. 8, elastic effects become more intense for higher values of Ka , which correspond to less viscous fluids and thinner films.

In Fig. 9 we present the effect of the Newtonian solvent viscosity in the viscoelastic fluid by increasing the parameter β of the ePTT model from 0 to 0.4. A zero value corresponds to the case of a polymer melt, whereas finite values of β represent the case of polymer solutions. Increase of β causes the peak on the relative amplitude to become less intense (for $\beta = 0$, A_{rel} was calculated to be 0.52 for $Re = 15.24$, while for $\beta = 0.4$ we get $A_{rel} = 0.48$ for $Re = 15.5$, see Fig. 9) as the liquid approaches Newtonian behavior. We have not considered values above $\beta = 0.4$, since in this case the liquid corresponds to dilute polymer solutions in which different phenomena may arise, such as polymer migration, that cannot be described by the ePTT model [32].

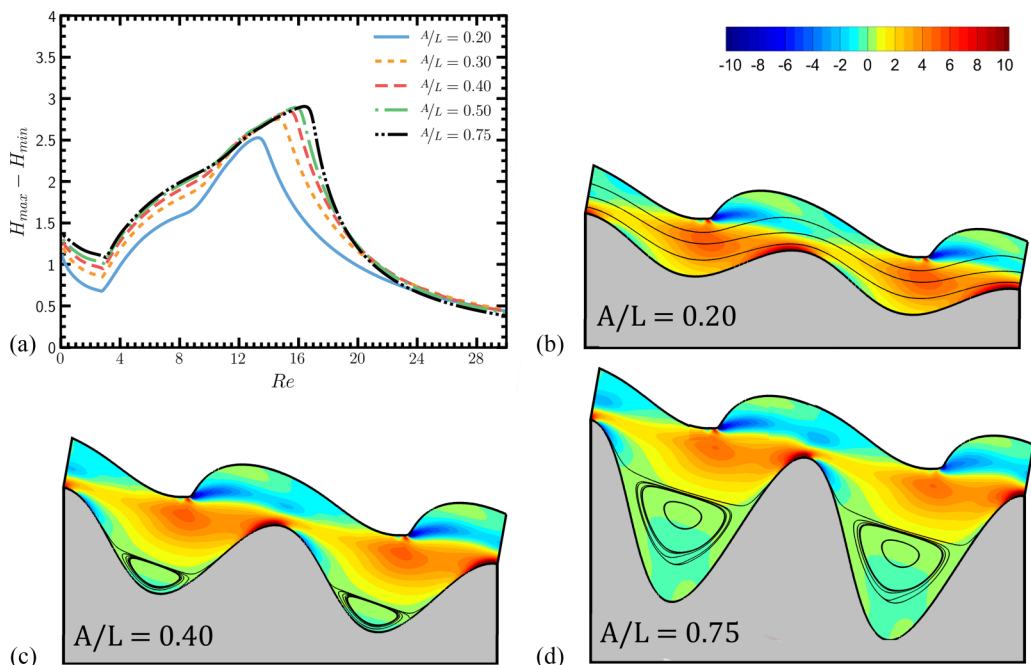


FIG. 10. (a) Free surface deformation as a function of the Reynolds number for various values of A . (b)–(d) Film shape and spatial variation of the shear stress component ($\tau_{p,yx}$) for $A = 2.7, 5.50, 10.30$ for $Re = 12.9, 14.6, 15.4$, respectively. The remaining parameters are $Wi = 1$, $\varepsilon = 0.25$, $\beta = 0.1$, and the inclination angle is set at $\alpha = 10^\circ$.

D. Effect of substrate geometry and inclination angle

Next we turn our attention to the effect of the geometrical characteristics on the flow. In Fig. 10 we examine the effect of increasing the amplitude of the substrate corrugations by keeping constant the value of $L = 13.765$ and varying the value of A . In Fig. 10(a) we present the variation of the amplitude of the interfacial deformation as a function of the Reynolds number. Here, we prefer to plot the term $H_{\max} - H_{\min}$ instead of the relative amplitude of the free surface, since A_{rel} tends to infinity as $A^* \rightarrow 0$. In Figs. 10(b)–10(d) we depict the film shape along with the streamlines and contour plots of the polymeric shear stress for $A = 2.70, 5.50$, and 10.30 , respectively. Note that the presented steady-state profiles were calculated at the peak of the amplitude of the free surface, see Fig. 10(a). For shallow wall corrugations, i.e., low values of A , the liquid experiences smaller interfacial deformations, see Fig. 10(a). As shown in Fig. 10(b), for $A = 2.70$, there is no recirculation and the flow remains attached to the bottom wall and as a result, the fluid flow is dominated by shear. In Fig. 10(b) we depict the polymeric shear stresses, which reach their maximum values at the ascending part of the wall and minimum at the vicinity of the free surface cusp. Note that the viscosity decreases considerably in the regions of high $\tau_{p,yx}$ values due to the shear thinning of the material. By increasing the amplitude of wall corrugations, interfacial deformation increases considerably [see Fig. 10(a)] while the flow detaches from the bottom part of the substrate undulations where a recirculating vortex arises, see Figs. 10(c) and 10(d). We observe, though, that the enhancement of the interfacial deformation saturates for very high amplitudes of the wall corrugations, see Fig. 10(a) for $A/L = 0.5, 0.75$. It is clear from this figure that for depths higher than $A/L = 0.75$ the maximum deformation of the free surface reaches an upper limit. This effect should be attributed to the presence of the recirculating vortex, as the main stream region of the film effectively does not feel the presence of the bottom wall, i.e., the generation of the eddy

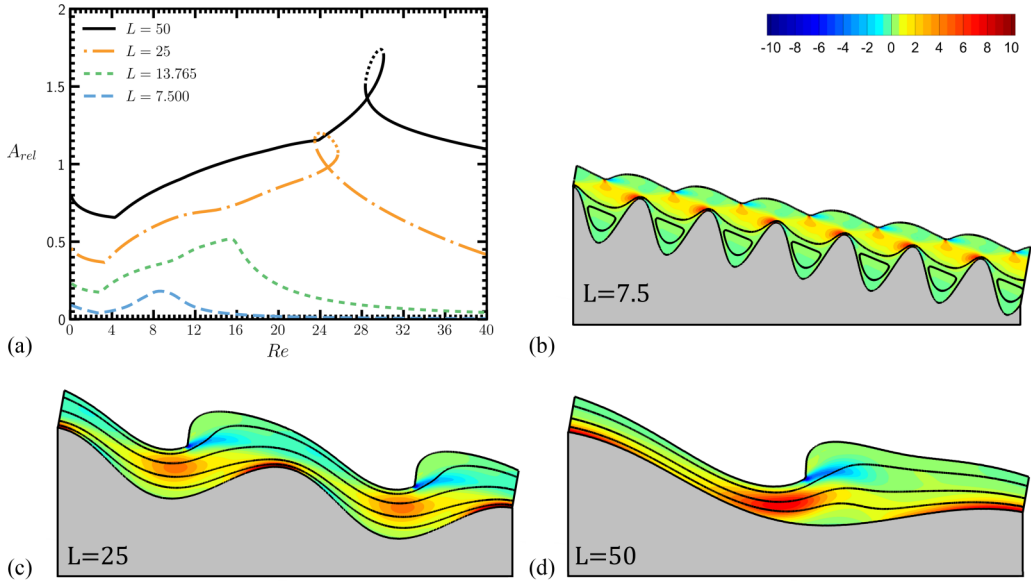


FIG. 11. (a) Relative amplitude of the free surface A_{rel} as a function of the Reynolds number for various values of L . (b)–(d) Film shape and spatial variation of the shear stress component $(\tau_{p,yx})$ for $L = 7.5, 25, 50$ for $Re = 8.5, 23.25, 24$, respectively. The remaining parameters are $Wi = 1$, $\varepsilon = 0.25$, and $\beta = 0.1$. The inclination angle is set at $\alpha = 10^\circ$.

in the midplane smooths out, in some sense, the undulations of the wall. Hence, as noted by [44] for Newtonian liquids, the separatrix line delivers an optimum substrate shape in a natural way. In the case of viscoelastic liquids, due to the presence of the recirculating vortex, the maximum values of the shear polymeric stress field are restricted closer to the crests of the topography, whereas the existence of the separatrix creates a liquid-liquid interface where the shear stresses obtain almost zero values. Thus, the existence of the recirculation induces an upper limit in the effect of shear thinning. It is worth noting that the film shapes along with the shear stress fields in Figs. 10(c) and 10(d) are almost identical.

Next we investigate the effect of the topography wavelength. In Fig. 11(a) we present the relative amplitude of the free surface deformation as a function of the Reynolds number for different values of L while keeping fixed the depth of the undulations at $A = 5.50$. For small values of L , the resonance of the steady free surface almost disappears, since the residence time inside the corrugations is small and the liquid does not have enough time to adjust to the shape of the wall and effectively feels as if it flows above a flat substrate. In the other limit, as L increases the film has more time to conform, leading to more intense resonance. Moreover, due to the fact that the flow is dominated by shear a hysteresis loop arises [see Figs. 11(c) and 11(d)] for $L = 25$ and 50 . In the case of Newtonian liquids, isolated standing waves have been documented by Wierschem and Aksel [45] (their Fig. 11) for flow along a wall with wavelength $L^* = 300$ mm and $A = 30$ mm in which the dimensionless forms are $L = 200$ and $A = 20$, respectively. However, in the presence of fluid elasticity the amplitude of this structure increases along with the cusp formation at the free surface, which is getting sharper.

So far, we have investigated a film flowing over a substrate inclined at 10 deg with respect to the horizontal position. To complete our parametric study, we examine in Fig. 12 the effect of the inclination angle α on the relative amplitude of the free surface as a function of Re . As α decreases, the y component of the gravity increases, increasing the pressure gradient in the same direction. Moreover, the Nusselt film thickness increases as the inclination angle decreases, as can be seen in

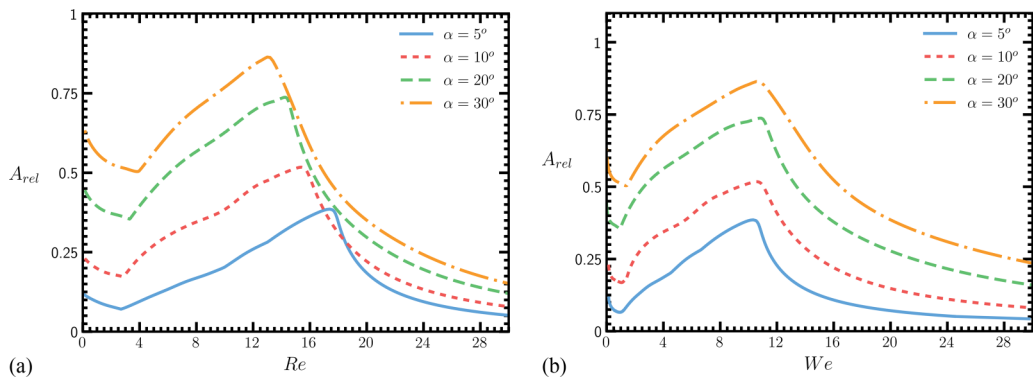


FIG. 12. Relative amplitude of the free surface A_{rel} as a function of (a) the Reynolds number and (b) Weber number for various values of inclination angles for $Wi = 1$, $\varepsilon = 0.25$, and $\beta = 0.1$.

Eq. (16). On the contrary, for higher inclination angles, since the flow is gravity driven, the velocity is higher and the film height decreases. Therefore, the deformations of the free surface decrease with decreasing α , and the maximum of A_{rel} is shifted to smaller Re values, see Fig. 12(a). Interestingly, plotting A_{rel} as a function of We [see Fig. 12(b)] we find that the point of resonance arises for different inclination angles at the same value of $We \approx 10$, confirming the finding of Fig. 7(b) that the resonance is caused by a delicate balance between inertia and surface tension.

VI. CONCLUSIONS

We studied the steady film flow of a viscoelastic fluid obeying the PTT constitutive law. To this end, we derived a computational model and solved the governing equations in 2D using the mixed finite-element method, while our code was extensively validated against previous theoretical and experimental studies concerning Newtonian materials that exist in the literature. We performed a thorough parametric analysis and examined the effect of the various geometrical characteristics of the flow as well as the rheological properties of the liquid and their interplay with inertia, viscous, and capillary forces.

It is shown that bulk elasticity at small flow rates suppresses interfacial deformations. At larger flow rates elasticity opposes fluid inertia, since the polymeric chains are extended in the direction of the fluid flow, creating a force that prevents the film from overpassing the wall undulations. As a result, the film shape creates a static hump and a cusp that precedes the free surface hump, close to the ascending part of the wall. The formation of the cusp is the outcome of the elastic rebound of the fluid from the wall and becomes more pronounced with increasing fluid elasticity. Due to the effect of shear thinning, the viscosity decreases locally, mostly near the substrate crests, which accelerates the flow and therefore inertia forces become more significant. At high flow rates, the increased effect of shear thinning promotes the decrease in the film thickness, leading to a more pronounced cusp at the interface. It is also found that the elastic phenomena are relaxed in the case of highly viscous liquids, as the films in this case are sufficiently thick, and the interface variations do not feel the presence of the substrate.

Regarding the effect of the geometric characteristics and the orientation of the substrate, we found that the creation of a recirculating vortex arising at the midplane of the substrate creates a natural boundary that damps the elastic phenomena that arise in the fluid flow. We found that there is a critical substrate depth above which the spatial variation of the stress field of the film flow remains unaffected. Furthermore, elastic effects appear to be more intense at large wavelengths of the substrate.

The present analysis is based on the usual steady-state assumption of the fluid flow over a sinusoidal substrate. This study leaves open the question about the stability of the computed steady solutions. Recently, Schörner *et al.* [46] combined experimental and numerical work to create stability maps for flow over substrates with topographical variations in the limit of Newtonian liquids. In general, they have shown that topographical variations stabilize the fluid flow, while they have revealed the existence of stable and unstable isles in the stability maps. On the other hand, the effect of elasticity over a flat substrate has been examined in detail by Shaqfeh *et al.* [47], who have shown that the effect of elasticity destabilizes the flow. The presence of topography will certainly complicate things even further. This will be the subject of Part II of this study [30], where we present a linear stability analysis considering as base state the steady solution that has been derived in this paper, by employing the Floquet-Bloch theory and assuming that the steady solution is subjected both to 2D and 3D disturbances of an arbitrary wavelength.

ACKNOWLEDGMENTS

The research work was supported by the Hellenic Foundation for Research and Innovation (HFRI) and the General Secretariat for Research and Technology (GSRT), under the HFRI PhD Fellowship grant (Grant Agreement No. 1473) and the LIMMAT Foundation under the grant MuSiComPS. G.K. would like to acknowledge Hellenic Foundation for Research and Innovation (HFRI) and the General Secretariat for Research and Technology (GSRT), under Grant Agreement No. 792.

APPENDIX: MIXED FINITE-ELEMENT METHOD–BASE STATE

We consider a 2D physical domain and flow field and approximate the velocity and the position vector with six-node Lagrangian basis functions ϕ^i , and the pressure, the elastic stresses, as well as the velocity gradients with three-node Lagrangian basis functions ψ^i :

$$\begin{bmatrix} \mathbf{u} \\ \mathbf{x} \end{bmatrix}(\eta, \xi) = \sum_i \begin{bmatrix} \mathbf{u}^i \\ \mathbf{x}^i \end{bmatrix} \phi^i(\eta, \xi) \text{ and } \begin{bmatrix} P \\ \mathbf{G} \\ \boldsymbol{\tau}_p \end{bmatrix}(\eta, \xi) = \sum_i \begin{bmatrix} P^i \\ \mathbf{G}^i \\ \boldsymbol{\tau}_p^i \end{bmatrix} \psi^i(\eta, \xi). \quad (\text{A1})$$

We employ the finite-element–Galerkin method, which after applying the divergence theorem results in the following weak form of the momentum and mass balances:

$$\int_{\Omega} [(\text{Re } \mathbf{u} \cdot \nabla \mathbf{u} - \text{St } \mathbf{g}) \cdot \mathbf{e}_j \phi^i - \mathbf{PI} : \nabla(\mathbf{e}_j \phi^i) + \boldsymbol{\tau}_{EVSS}^T : \nabla(\mathbf{e}_j \phi^i)] J_{2D} d\Omega - \int_{\partial\Omega} \mathbf{n} \cdot (-\mathbf{PI} + \boldsymbol{\tau}_{EVSS}) \cdot \mathbf{e}_j \phi^i J_{1D} d\Gamma = 0, \quad j = x, y, \quad (\text{A2})$$

$$\int_{\Omega} \psi^i \nabla \cdot \mathbf{u} J_{2D} d\Omega = 0, \quad (\text{A3})$$

where $d\Omega = d\eta d\xi$ and $d\Gamma$ are the differential area and arc length in the computational domain, respectively, while $J_{2D} = y_{\xi} x_{\eta} - y_{\eta} x_{\xi}$ and $J_{1D} = \sqrt{x_{\Gamma}^2 + y_{\Gamma}^2}$ denote the corresponding Jacobians of the transformation from physical to computational domain. The weak form of the mesh generation equations is derived similarly by applying the divergence theorem:

$$\int_e \nabla \phi^i \cdot \nabla \xi [(1 - \varepsilon_1) + \varepsilon_1 S] J_{2D} d\Omega = 0, \quad (\text{A4})$$

$$\int_e \nabla \phi^i \cdot \nabla \eta J_{2D} d\Omega = 0, \quad (\text{A5})$$

where $S = \sqrt{(x_{\xi}^2 + y_{\xi}^2)/(x_{\eta}^2 + y_{\eta}^2)}$, and ε_1 is a parameter that controls the smoothness of the mapping relative to the degree of orthogonality of the mesh lines; here we set $\varepsilon_1 = 0.1$. For a more detailed description of this method, the interested reader may refer to [40,48–52].

The continuous approximation of the components of the velocity gradient is determined by

$$\int_e \psi^i (\mathbf{G} - \nabla \mathbf{u}) J_{2D} d\Omega = 0. \quad (\text{A6})$$

Finally, the hyperbolic character of the constitutive equation necessitates discretizing it using the SUPG method proposed by [36]

$$\int_e \chi^i [Y(\boldsymbol{\tau}_p) \boldsymbol{\tau}_p + \text{Wi} \overset{\nabla}{\boldsymbol{\tau}}_p - (1 - \beta)(\mathbf{G} + \mathbf{G}^T)] J_{2D} d\Omega = 0, \quad (\text{A7})$$

where $\overset{\nabla}{\boldsymbol{\tau}}_p = \mathbf{u} \cdot \nabla \boldsymbol{\tau}_p - \boldsymbol{\tau}_p \cdot \mathbf{G} - (\boldsymbol{\tau}_p \cdot \mathbf{G})^T$. The weighting function χ^i is formed from the finite-element basis function for the elastic stress components according to

$$\chi^i = \psi^i + \frac{h_{ch}}{|\mathbf{u}|} \mathbf{u} \cdot \nabla \psi^i, \quad (\text{A8})$$

where $|\mathbf{u}|$ is the magnitude of the mean velocity and h_{ch} is a characteristic length in each element.

The mean velocity $|\mathbf{u}|$ in an element is defined as $|\mathbf{u}| = \frac{1}{3} \sum_{n=1}^3 |\mathbf{u}|_n$, $|\mathbf{u}|_n$ denoting the magnitude of the velocity at the vertices of the corresponding triangular element. As a characteristic length h_{ch} , we used the square root of the area of each triangular element.

-
- [1] R. V. Craster and O. K. Matar, Dynamics and stability of thin liquid films, *Rev. Mod. Phys.* **81**, 1131 (2009).
 - [2] L. E. Stillwagon and R. G. Larson, Leveling of thin films over uneven substrates during spin coating, *Phys. Fluids A* **2**, 1937 (1990).
 - [3] X. Yin and S. Kumar, Two-dimensional simulations of flow near a cavity and a flexible solid boundary, *Phys. Fluids* **18**, 063103 (2006).
 - [4] K. Argyriadi, M. Vlachogiannis, and V. Bontozoglou, Experimental study of inclined film flow along periodic corrugations: The effect of wall steepness, *Phys. Fluids* **18**, 012102 (2006).
 - [5] N. J. Balmforth, R. V. Craster, A. C. Rust, and R. Sassi, Viscoplastic flow over an inclined surface, *J. Non-Newtonian Fluid Mech.* **139**, 103 (2006).
 - [6] D. Bonn, J. Eggers, J. Indekeu, J. Meunier, and E. Rolley, Wetting and spreading, *Rev. Mod. Phys.* **81**, 739 (2009).
 - [7] M. M. J. Decre and J.-C. Baret, Gravity-driven flows of viscous liquids over two-dimensional topographies, *J. Fluid Mech.* **487**, 147 (2003).
 - [8] M. Scholle, A. Haas, N. Aksel, M. C. T. Wilson, H. M. Thompson, and P. H. Gaskell, Competing geometric and inertial effects on local flow structure in thick gravity-driven fluid films, *Phys. Fluids* **20**, 123101 (2008).
 - [9] M. I. Pak and G. H. Hu, Numerical investigations on vortical structures of viscous film flows along periodic rectangular corrugations, *Int. J. Multiphase Flow* **37**, 369 (2011).
 - [10] P. H. Gaskell, P. K. Jimack, M. Sellier, H. M. Thompson, and M. C. T. Wilson, Gravity-driven flow of continuous thin liquid films on non-porous substrates with topography, *J. Fluid Mech.* **509**, 253 (2004).
 - [11] S. Kalliadasis, C. Bielarz, and G. M. Homsy, Steady free-surface thin film flows over topography, *Phys. Fluids* **12**, 1889 (2000).
 - [12] A. Mazouchi and G. M. Homsy, Free surface Stokes flow over topography, *Phys. Fluids* **13**, 2751 (2001).
 - [13] C. Pozrikidis, The flow of a liquid film along a periodic wall, *J. Fluid Mech.* **188**, 275 (1988).
 - [14] M. G. Blyth and C. Pozrikidis, Film flow down an inclined plane over a three-dimensional obstacle, *Phys. Fluids* **18**, 052104 (2006).

- [15] S. Kalliadasis and G. M. Homsy, Stability of free-surface thin-film flows over topography, *J. Fluid Mech.* **448**, 387 (2001).
- [16] S. Veremieiev, H. M. Thompson, Y. C. Lee, and P. H. Gaskell, Inertial thin film flow on planar surfaces featuring topography, *Comput. Fluids* **39**, 431 (2010).
- [17] V. Bontozoglou and K. Serifi, Falling film flow along steep two-dimensional topography: The effect of inertia, *Int. J. Multiphase Flow* **34**, 734 (2008).
- [18] A. Wierschem, V. Bontozoglou, C. Heining, H. Uecker, and N. Aksel, Linear resonance in viscous films on inclined wavy planes, *Int. J. Multiphase Flow* **34**, 580 (2008).
- [19] P.-K. Nguyen and V. Bontozoglou, Steady solutions of inertial film flow along strongly undulated substrates, *Phys. Fluids* **23**, 052103 (2011).
- [20] C. Heining, V. Bontozoglou, N. Aksel, and A. Wierschem, Nonlinear resonance in viscous films on inclined wavy planes, *Int. J. Multiphase Flow* **35**, 78 (2009).
- [21] D. Tseluiko, M. G. Blyth, and D. T. Papageorgiou, Stability of film flow over inclined topography based on a long-wave nonlinear model, *J. Fluid Mech.* **729**, 638 (2013).
- [22] D. Pettas, G. Karapetsas, Y. Dimakopoulos, and J. Tsamopoulos, On the degree of wetting of a slit by a liquid film flowing along an inclined plane, *J. Fluid Mech.* **820**, 5 (2017).
- [23] N. K. Lampropoulos, Y. Dimakopoulos, and J. Tsamopoulos, Transient flow of gravity-driven viscous films over substrates with rectangular topographical features, *Microfluid. Nanofluid.* **20**, 51 (2016).
- [24] G. Karapetsas, N. K. Lampropoulos, Y. Dimakopoulos, and J. Tsamopoulos, Transient flow of gravity-driven viscous films over 3D patterned substrates: Conditions leading to Wenzel, Cassie and intermediate states, *Microfluid. Nanofluid.* **21**, 17 (2017).
- [25] S. Varchanis, Y. Dimakopoulos, and J. Tsamopoulos, Steady film flow over a substrate with rectangular trenches forming air inclusions, *Phys. Rev. Fluids* **2**, 124001 (2017).
- [26] S. Saprykin, R. J. Koopmans, and S. Kalliadasis, Free-surface thin-film flows over topography: influence of inertia and viscoelasticity, *J. Fluid Mech.* **578**, 271 (2007).
- [27] M. Pavlidis, Y. Dimakopoulos, and J. Tsamopoulos, Steady viscoelastic film flow over 2D topography: I. The effect of viscoelastic properties under creeping flow, *J. Non-Newtonian Fluid Mech.* **165**, 576 (2010).
- [28] M. Pavlidis, G. Karapetsas, Y. Dimakopoulos, and J. Tsamopoulos, Steady viscoelastic film flow over 2D Topography: II. The effect of capillarity, inertia and substrate geometry, *J. Non-Newtonian Fluid Mech.* **234**, 201 (2016).
- [29] N. Phan-Thien, A nonlinear network viscoelastic model, *J. Rheol.* **22**, 259 (1978).
- [30] D. Pettas, G. Karapetsas, Y. Dimakopoulos, and J. Tsamopoulos, Viscoelastic film flows over an inclined substrate with sinusoidal topography. II. Linear stability analysis, *Phys. Rev. Fluids* **4**, 083304 (2019).
- [31] T. Pollak and N. Aksel, Crucial flow stabilization and multiple instability branches of gravity-driven films over topography, *Phys. Fluids* **25**, 024103 (2013).
- [32] S. Tsouka, Y. Dimakopoulos, and J. Tsamopoulos, Stress-gradient induced migration of polymers in thin films flowing over smoothly corrugated surfaces, *J. Non-Newtonian Fluid Mech.* **228**, 79 (2016).
- [33] G. Karapetsas and J. Tsamopoulos, On the stick-slip flow from slit and cylindrical dies of a Phan-Thien and Tanner fluid model. II. Linear stability analysis, *Phys. Fluids* **25**, 093105 (2013).
- [34] Y. Trifonov, Stability of a film flowing down an inclined corrugated plate: The direct Navier-Stokes computations and Floquet theory, *Phys. Fluids* **26**, 114101 (2014).
- [35] F. P. T. Baaijens, Mixed finite element methods for viscoelastic flow analysis: A review, *J. Non-Newtonian Fluid Mech.* **79**, 361 (1998).
- [36] A. Brooks and T. J. R. Hughes, Streamline upwind/Petrov-Galerkin formulations for convection dominated flows with particular emphasis on the incompressible Navier-Stokes equations, *Comput. Methods Appl. Mech. Eng.* **32**, 199 (1982).
- [37] N. Chatzidai, A. Giannousakis, Y. Dimakopoulos, and J. Tsamopoulos, On the elliptic mesh generation in domains containing multiple inclusions and undergoing large deformations, *J. Comput. Phys.* **228**, 1980 (2009).
- [38] D. Pettas, G. Karapetsas, Y. Dimakopoulos, and J. Tsamopoulos, On the origin of extrusion instabilities: Linear stability analysis of the viscoelastic die swell, *J. Non-Newtonian Fluid Mech.* **224**, 61 (2015).

- [39] G. Karapetsas and V. Bontozoglou, Non-linear dynamics of a viscoelastic film subjected to a spatially periodic electric field, *J. Non-Newtonian Fluid Mech.* **217**, 1 (2015).
- [40] Y. Dimakopoulos and J. Tsamopoulos, A quasi-elliptic transformation for moving boundary problems with large anisotropic deformations, *J. Comput. Phys.* **192**, 494 (2003).
- [41] M. Vlachogiannis and V. Bontozoglou, Experiments on laminar film flow along a periodic wall, *J. Fluid Mech.* **457**, 133 (2002).
- [42] V. Bontozoglou and G. Papapolymerou, Wall-triggered interfacial resonance in laminar gas-liquid flow, *Int. J. Multiph. Flow* **23**, 131 (1997).
- [43] C. Heining and N. Aksel, Effects of inertia and surface tension on a power-law fluid flowing down a wavy incline, *Int. J. Multiphase Flow* **36**, 847 (2010).
- [44] M. Schörner, D. Reck, and N. Aksel, Does the topography's specific shape matter in general for the stability of film flows? *Phys. Fluids* **27**, 042103 (2015).
- [45] A. Wierschem and N. Aksel, Hydraulic jumps and standing waves in gravity-driven flows of viscous liquids in wavy open channels, *Phys. Fluids* **16**, 3868 (2004).
- [46] M. Schörner, D. Reck, N. Aksel, and Y. Trifonov, Switching between different types of stability isles in films over topographies, *Acta Mech.* **229**, 423 (2017).
- [47] E. S. G. Shaqfeh, R. G. Larson, and G. H. Fredrickson, The stability of gravity driven viscoelastic film-flow at low to moderate Reynolds number, *J. Non-Newton. Fluid Mech.* **31**, 87 (1989).
- [48] K. N. Christodoulou, Computational physics of slide coating flow, Volumes I and II, Ph.D. Thesis, University of Minnesota, 1990.
- [49] K. N. Christodoulou and L. E. Scriven, Finding leading modes of a viscous free surface flow: An asymmetric generalized eigenproblem, *J. Sci. Comput.* **3**, 355 (1988).
- [50] K. Tsiveriotis and R. A. Brown, Boundary-conforming mapping applied to computations of highly deformed solidification interfaces, *Int. J. Numer. Methods Fluids* **14**, 981 (1992).
- [51] D. Fragedakis, J. Papaioannou, Y. Dimakopoulos, and J. Tsamopoulos, Discretization of three-dimensional free surface flows and moving boundary problems via elliptic grid methods based on variational principles, *J. Comput. Phys.* **344**, 127 (2017).
- [52] Y. Dimakopoulos and J. Tsamopoulos, Transient displacement of Newtonian and viscoplastic liquids by air in complex tubes, *J. Non-Newtonian Fluid Mech.* **142**, 162 (2007).